

A viscoelastic nonlinear energy sink with an electromagnetic energy harvester: Narrow-band random response

Zhi-Jing Liao(廖志晶), Ya-Hui Sun(孙亚辉), and Yang Liu(刘洋)

Citation: Chin. Phys. B, 2024, 33 (**7**): 070205. DOI: 10.1088/1674-1056/ad4632
Journal homepage: http://cpb.iphy.ac.cn; http://iopscience.iop.org/cpb

What follows is a list of articles you may be interested in

Performance enhancement of a viscoelastic bistable energy harvester using time-delayed feedback control

Mei-Ling Huang(黄美玲), Yong-Ge Yang(杨勇歌), and Yang Liu(刘洋)
Chin. Phys. B, 2024, 33 (**6**): 060203. DOI: 10.1088/1674-1056/ad3b89

Dynamic responses of an energy harvesting system based on piezoelectric and electromagnetic mechanisms under colored noise

Yong-Ge Yang(杨勇歌), Yun Meng(孟运), Yuan-Hui Zeng(曾远辉), and Ya-Hui Sun(孙亚辉)
Chin. Phys. B, 2023, 32 (**9**): 090201. DOI: 10.1088/1674-1056/acd621

Mutation detection and fast identification of switching system based on data-driven method

Zhonghua Zhang(张钟化), Wei Xu(徐伟), and Yi Song(宋怡)
Chin. Phys. B, 2023, 32 (**5**): 050201. DOI: 10.1088/1674-1056/acb9f5

Inhibitory effect induced by fractional Gaussian noise in neuronal system

Zhi-Kun Li(李智坤) and Dong-Xi Li(李东喜)
Chin. Phys. B, 2023, 32 (**1**): 010203. DOI: 10.1088/1674-1056/ac6332

Sparse identification method of extracting hybrid energy harvesting system from observed data

Ya-Hui Sun(孙亚辉), Yuan-Hui Zeng(曾远辉), and Yong-Ge Yang(杨勇歌)
Chin. Phys. B, 2022, 31 (**12**): 120203. DOI: 10.1088/1674-1056/ac9cbf

---

A viscoelastic nonlinear energy sink with an electromagnetic energy harvester: Narrow-band random response

Zhi-Jing Liao(廖志晶)[1], Ya-Hui Sun(孙亚辉)[1,2,†], and Yang Liu(刘洋)[2]

[1] *School of Mathematics and Statistics, Guangdong University of Technology, Guangzhou* 510520, *China*
[2] *Exeter Small-Scale Robotics Laboratory, Engineering Department, University of Exeter, North Park Road, Exeter EX*4 4*QF, UK*

(Received 30 March 2024; revised manuscript received 24 April 2024; accepted manuscript online 2 May 2024)

Nonlinear energy sink is a passive energy absorption device that surpasses linear dampers, and has gained significant attention in various fields of vibration suppression. This is owing to its capacity to offer high vibration attenuation and robustness across a wide frequency spectrum. Energy harvester is a device employed to convert kinetic energy into usable electric energy. In this paper, we propose an electromagnetic energy harvester enhanced viscoelastic nonlinear energy sink (VNES) to achieve passive vibration suppression and energy harvesting simultaneously. A critical departure from prior studies is the investigation of the stochastic P-bifurcation of the electromechanically coupled VNES system under narrow-band random excitation. Initially, approximate analytical solutions are derived using a combination of a multiple-scale method and a perturbation approach. The substantial agreement between theoretical analysis solutions and numerical solutions obtained from Monte Carlo simulation underscores the method's high degree of validity. Furthermore, the effects of system parameters on system responses are carefully examined. Additionally, we demonstrate that stochastic P-bifurcation can be induced by system parameters, which is further verified by the steady-state density functions of displacement. Lastly, we analyze the impacts of various parameters on the mean square current and the mean output power, which are crucial for selecting suitable parameters to enhance the energy harvesting performance.

Keywords: nonlinear energy sink, fractional-order damping, multiple-scale method, energy harvester

PACS: 02.50.–r, 05.40.–a, 05.40.Ca **DOI:** 10.1088/1674-1056/ad4632

1. Introduction

To mitigate the limitations of linear dampers, which typically have a narrow vibration suppression frequency band, a series of passive vibration absorbers have been proposed.[1–5] One such absorber is the nonlinear energy sink (NES), a passive vibration suppression device composed of mass, nonlinear stiffness and damping components.[6–9] NESs have found widespread applications across engineering fields due to their effectiveness in attenuating vibration over a broad frequency range and facilitating targeted energy transfer.[10,11] To date, numerous types of NESs have been designed and implemented.[12–14] Some scholars have explored the possibility of achieving enhanced vibration reduction by increasing the number of NES units.[15] Ding *et al.*[16] firstly put forward the concept of NES cell and have improved the reliability of NES and its versatility to complex vibration structures by adding a large number of NES cells in parallel. Additionally, considerable attention has been devoted to studying the dynamic response of systems coupled with NESs under conditions of random or harmonic excitation. For example, Zhang *et al.*[17] proposed a new NES to control vertical system vibration subjected to harmonic and shock excitations. Through comparative analysis of the dynamic responses of different NES configurations under varying impulsive load amplitudes, Zhang *et al.*[18] concluded that NESs with combined damping yield the most effective vibration suppression. Li *et al.*[19] determined threshold values for external excitation amplitude and frequency necessary for NESs to achieve effective vibration suppression. Gaidai *et al.*[20] investigated targeted energy transfer in stochastic systems under Gaussian white noise excitation. Bergeot *et al.*[21] employed stochastic averaging methods to study the slow flow of a stochastically forced self-sustained oscillator coupled to an NES. However, compared to random or harmonic excitation, narrow-band random excitation presents more complex modeling challenges, closely resembling real-world scenarios and exhibiting more intricate dynamic behavior. This observation motivates us to consider narrow-band random excitation in our study.

Reviewing prior studies reveals that enhancing the resilience of nonlinear restoring forces can lead to improved vibration suppression performance. Consequently, the role of damping becomes crucial in achieving vibration attenuation within NES systems. Viscoelastic materials, distinguished by their combined viscosity and elasticity, offer significant potential for effective vibration and noise reduction across a broad frequency spectrum.[22–24] Hence, there has been considerable scholarly interest in exploring the application of viscoelastic materials for structural vibration attenuation. Fractional-order damping offers greater flexibility and enables a more accurate depiction of the dynamic behavior of complex systems compared to integer-order damping in system modeling. For ex-

[†]Corresponding author. E-mail: yahsun@163.com

© 2024 Chinese Physical Society and IOP Publishing Ltd

ample, Huang *et al.*[25] studied the dynamic response of a viscoelastic isolation system coupled with nonlinear energy sinks using the complexification-averaging method. Hu *et al.*[26] conducted a study on random vibration analysis of nonlinear oscillator equipped with a viscoelastic nonlinear energy sink, employing the stochastic averaging method. Moslemi *et al.*[27] identified that viscoelasticity can impact the frequency interval between Hopf and saddle-node branches. Ultimately, this paper adopted a viscoelastic nonlinear energy sink (VNES) model to address these considerations.

Vibration energy harvesters have seen significant advancements owing to their ability to convert kinetic energy to useful electrical energy, addressing power supply challenges. Various types of energy harvesters have been developed, including piezoelectric,[28] electromagnetic,[29] electrostatic,[30] and piezoelectric–electromagnetic hybrid types.[31] Han *et al.*[32] obtained the moments of the stochastic galloping energy harvester with a parallel circuit. Huang *et al.*[33] studied responses, optimization and prediction of energy harvesters under galloping and base excitations by using the complexification-averaging method. Recently, scholars have explored the integration of NESs with energy harvesters for structural vibration reduction and energy harvesting. For example, Franzini *et al.*[34] employed a bistable piezoelectric NES for both vibration reduction and energy harvesting within a system. Zhang *et al.*[35] experimentally verified the application of NES and piezoelectric energy harvester for flutter suppression in airfoil structures. Li *et al.*[36] investigated the effects of a nonlinear device for simultaneous vibration absorption and energy harvesting. Electromagnetic energy harvesters have demonstrated high conversion efficiency and operability across a wide frequency range. Despite this, research on combining VNES with electromagnetic energy harvesters for vibration suppression and energy harvesting remains limited. From a systematic energy and performance point of view, integrating VNES with electromagnetic energy harvester holds significant promise as it enables the effective utilization of structural vibration energy and enhances structural stability.

The dynamic behavior of a system undergoes changes in response to variations in its parameters, a phenomenon known as bifurcation. The occurrence of bifurcation indicates the instability of the system. Examining the critical parameter values at which bifurcation occurs aids in understanding the system's evolutionary pattern and offers insights for system control. Starosvetsky *et al.*[37] demonstrated through numerical analysis that when the quality of the NES decreases sufficiently, the system enters a strongly modulated response regime. Zang *et al.*[38] studied bifurcation phenomena in a structure coupled with a lever-type NES. Similarly, Mirhashemi *et al.*[39] conducted a numerical analysis of bifurcations in a harmonically excited nonlinear system equipped with a local NES. Sun *et al.*[40] analyzed stochastic P-bifurcation of a fractional-order damping system coupled with a nonlinear energy sink excited by Gaussian white noise and obtained the critical conditions of stochastic P-bifurcation. In this paper, we discuss the critical parameter values associated with stochastic P-bifurcation using numerical methods.

The rest of this paper is organized as follows. In Section 2, we present the mathematical model and simplifications of the system. Section 3 provides the first and second steady-state moments of the system obtained using the multiple-scale method. The effectiveness of the adopted approach is verified in Section 4. Additionally, Section 4 discusses stochastic P-bifurcation and energy harvesting performance. Finally, Section 5 presents the conclusions drawn from our study.

2. Mathematical modeling and simplification

The model of an electromechanically coupled VNES is described in Fig. 1, which consists of a primary structure coupled to VNES by an electromagnetic device. The electromechanically coupled VNES under narrow-band random excitation can be expressed as the following general form:

$$\begin{aligned}
&m_1\ddot{X}_1 + c_1\dot{X}_1 + k_1X_1 - k_{\mathrm{n}}X_2^3 - c_{\mathrm{n}}D^{\mu}X_2 \\
&-c_2\dot{X}_2 - \rho_1 I = -m_1\ddot{X}, \\
&m_2(\ddot{X}_1 + \ddot{X}_2) + k_{\mathrm{n}}X_2^3 + c_{\mathrm{n}}D^{\mu}X_2 + \rho_1 I = -m_2\ddot{X}, \\
&L\dot{I} + (R_I + R_L)I = \rho_1\dot{X}_2,
\end{aligned} \tag{1}$$

where m_1 and m_2 are the masses of the primary structure and VNES. X_1 is the relative displacement between the primary structure and the base. X_2 is the relative displacement between VNES and the primary structure. k_1 and c_1 are the linear stiffness and linear damping coefficients of the primary structure. k_{n}, c_{n} and c_2 are the cubic stiffness, fractional-order damping and linear damping coefficients of VNES. ρ_1, I, R_I, R_L, and L denote the electromagnetic coupling coefficient, the output current, the load resistance, the resistance of the coil, and the inductance of the electromagnetic circuit, respectively. $\ddot{X} = h\cos(\Omega t + \gamma W(t))$ denotes narrow-band random excitation, where h and Ω are the amplitude and frequency of the excitation. γ is the intensity of Gaussian white noise $W(t)$. μ is the fractional derivative order. $D^{\mu}X(t)$ is a Caputo fractional derivative defined as

$$D^{\mu}X(t) = \frac{1}{\Gamma(1-\mu)}\int_0^t \frac{\dot{X}(s)}{(t-s)^{\mu}}\,\mathrm{d}s, \quad 0 < \mu < 1. \tag{2}$$

Introducing the following non-dimensional parameters:

$$x_1 = \frac{X_1}{l}, \quad x_2 = \frac{X_2}{l}, \quad \overline{F} = \frac{h}{l\omega_0^2}, \quad \tau = \omega_0 t, \quad \omega = \frac{\Omega}{\omega_0},$$

$$\overline{\sigma} = 1 - \omega^2, \quad \omega_0 = \sqrt{\frac{k_1}{m_1}}, \quad \rho = \frac{m_2}{m_1}, \quad \overline{d_1} = \frac{c_1}{m_1\omega_0},$$

$$\overline{d_2} = \frac{k_{\mathrm{n}}l^2}{m_1\omega_0^2}, \quad \overline{d_3} = \frac{c_{\mathrm{n}}}{m_1\omega_0}, \quad \overline{d_4} = \frac{c_2}{m_1\omega_0}, \quad \overline{\lambda} = \frac{\rho_1}{m_1 l\omega_0^2},$$

$$\zeta_1 = \frac{R_I + R_L}{L}, \quad \zeta_2 = \frac{\rho_1 l \omega_0}{L}. \tag{3}$$

The governing equations given by Eq. (1) can be rewritten as

$$\begin{aligned}
&\ddot{x}_1 + \overline{d_1}\dot{x}_1 + (\omega^2 + \overline{\sigma})x_1 - \overline{d_2}x_2^3 - \overline{d_3}D^{\mu}x_2 - \overline{d_4}\dot{x}_2 - \overline{\lambda}I \\
&= -\overline{F}\cos(\omega\tau + \gamma W(\tau)), \\
&\rho(\ddot{x}_1 + \ddot{x}_2) + \overline{d_2}x_2^3 + \overline{d_3}D^{\mu}x_2 + \overline{d_4}\dot{x}_2 + \overline{\lambda}I \\
&= -\rho\overline{F}\cos(\omega\tau + \gamma W(\tau)), \\
&\dot{I} + \zeta_1 I - \zeta_2\dot{x}_2 = 0,
\end{aligned} \tag{4}$$

in which x_1 and x_2 represent the displacements of the primary structure and VNES, respectively. $\dot{x}_1$ and $\dot{x}_2$ denote the velocities of the primary structure and VNES, respectively. l is the length scale. ρ is the mass ratio of VNES to the primary structure. $\overline{d_1}$ and $\overline{d_4}$ are the dimensionless linear damping coefficients of the primary structure and VNES, respectively. $\overline{d_2}$, $\overline{d_3}$, ω, and $\overline{\sigma}$ are the nondimensional cubic stiffness coefficient, the nondimensional fractional-order damping coefficient, the forcing frequency, and the detuning frequency, respectively. $\overline{F}$, $\overline{\lambda}$, ζ_1, and ζ_2 represent the deterministic amplitude, the electromechanical coupling coefficient, the ratio between resistance and inductance, and the dimensionless electromagnetic coupling coefficient, respectively.

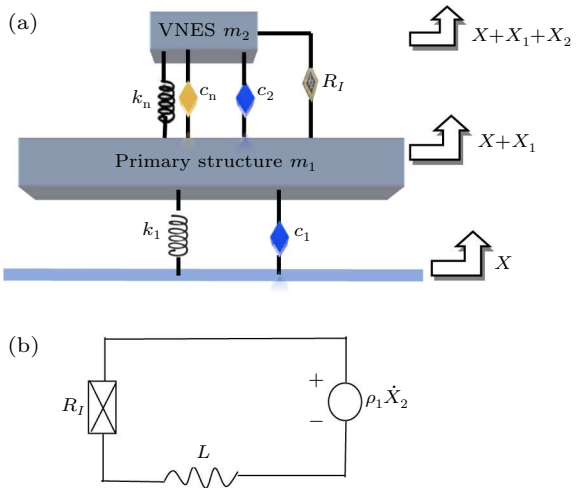


Fig. 1. The simplified structure of VNES with an electromagnetic energy harvester: (a) mechanical schematic, (b) equivalent circuit for electromagnetic mechanism.

To apply the multiple-scale method,[41–43] equation (4) is scaled with a small parameter ε to yield

$$\begin{aligned}
&\ddot{x}_1 + \varepsilon d_1\dot{x}_1 + (\omega^2 + \varepsilon\sigma)x_1 - \varepsilon d_2 x_2^3 - \varepsilon d_3 D^{\mu}x_2 \\
&-\varepsilon d_4\dot{x}_2 - \varepsilon\lambda I = -\varepsilon F\cos(\omega\tau + \gamma W(\tau)), \\
&\varepsilon\rho(\ddot{x}_1 + \ddot{x}_2) + \varepsilon d_2 x_2^3 + \varepsilon d_3 D^{\mu}x_2 \\
&+\varepsilon d_4\dot{x}_2 + \varepsilon\lambda I = -\varepsilon\rho F\cos(\omega\tau + \gamma W(\tau)), \\
&\varepsilon\dot{I} + \varepsilon\zeta_1 I - \varepsilon\zeta_2\dot{x}_2 = 0.
\end{aligned} \tag{5}$$

Pay attention to the contribution of viscoelastic damping to the recovery and dissipation terms of the system. Rely on the detailed derivations in Ref. [44], $D^{\mu}x_2(\tau)$ can be decoupled into the following two terms:

$$d_3 D^{\mu}x_2(\tau) = e_1\dot{x}_2(\tau) + f x_2(\tau), \tag{6}$$

in which $e_1 = d_3 k^{\mu-1}\sin\frac{\mu\pi}{2}$, $f = d_3 k^{\mu}\cos\frac{\mu\pi}{2}$, and k is the averaged frequency of the system.

Substituting Eq. (6) into Eq. (5), an equivalent nonlinear stochastic system can be derived as

$$\begin{aligned}
&\ddot{x}_1 + \varepsilon d_1\dot{x}_1 + (\omega^2 + \varepsilon\sigma)x_1 - \varepsilon d_2 x_2^3 - \varepsilon e\dot{x}_2 - \varepsilon f x_2 - \varepsilon\lambda I \\
&= -\varepsilon F\cos(\omega\tau + \gamma W(\tau)), \\
&\varepsilon\rho(\ddot{x}_1 + \ddot{x}_2) + \varepsilon d_2 x_2^3 + \varepsilon e\dot{x}_2 + \varepsilon f x_2 + \varepsilon\lambda I \\
&= -\varepsilon\rho F\cos(\omega\tau + \gamma W(\tau)), \\
&\varepsilon\dot{I} + \varepsilon\zeta_1 I - \varepsilon\zeta_2\dot{x}_2 = 0,
\end{aligned} \tag{7}$$

where $e = e_1 + d_4$.

3. Stochastic response analysis

Following the multiple-scale method, the solutions of Eq. (7) can be expressed as follows:

$$\begin{aligned}
x_1 &= x_{10}(T_0, T_1) + \varepsilon x_{11}(T_0, T_1) + \varepsilon^2 x_{12}(T_0, T_1) + O(\varepsilon^3), \\
x_2 &= x_{20}(T_0, T_1) + \varepsilon x_{21}(T_0, T_1) + \varepsilon^2 x_{22}(T_0, T_1) + O(\varepsilon^3), \\
I &= I_0(T_0, T_1) + \varepsilon I_1(T_0, T_1) + \varepsilon^2 I_2(T_0, T_1) + O(\varepsilon^3),
\end{aligned} \tag{8}$$

where the fast and slow time scales $T_0 = \tau$ and $T_1 = \varepsilon\tau$. Introducing the differential operators $D_0 = \partial/\partial T_0$, $D_1 = \partial/\partial T_1$, the time derivatives become

$$\begin{cases}
\dfrac{\mathrm{d}}{\mathrm{d}\tau} = D_0 + \varepsilon D_1 + O(\varepsilon^2), \\
\dfrac{\mathrm{d}^2}{\mathrm{d}\tau^2} = D_0^2 + 2\varepsilon D_0 D_1 + O(\varepsilon^2).
\end{cases} \tag{9}$$

Substituting Eqs. (8) and (9) into Eq. (7) and equating the same order of ε lead to the following set of equations. Order ε^0:

$$D_0^2 x_{10} + \omega^2 x_{10} = 0. \tag{10}$$

Order ε^1:

$$\begin{aligned}
&D_0^2 x_{11} + \omega^2 x_{11} + \sigma x_{10} + d_1 D_0 x_{10} + 2D_0 D_1 x_{10} - f x_{20} \\
&-d_2 x_{20}^3 - e D_0 x_{20} - \lambda I_0 + F\cos(\omega T_0 + \gamma W(T_1)) = 0,
\end{aligned} \tag{11a}$$

$$\begin{aligned}
&\rho(D_0^2 x_{10} + D_0^2 x_{20}) + f x_{20} + d_2 x_{20}^3 \\
&+e D_0 x_{20} + \lambda I_0 = -\rho F\cos(\omega T_0 + \gamma W(T_1)),
\end{aligned} \tag{11b}$$

$$D_0 I_0 + \zeta_1 I_0 - \zeta_2 D_0 x_{20} = 0. \tag{11c}$$

Order ε^2:

$$\begin{aligned}
&D_0^2 x_{12} + \omega^2 x_{12} + \sigma x_{11} + d_1 D_0 x_{11} + d_1 D_1 x_{10} \\
&+D_1^2 x_{10} + 2D_0 D_1 x_{11} - e D_0 x_{21} - e D_1 x_{20}
\end{aligned}$$

$$-fx_{21}-3d_2x_{20}^2x_{21}-\lambda I_1=0, \tag{12a}$$

$$\rho(D_0^2x_{21}+D_0^2x_{11})+2\rho D_1D_0(x_{10}+x_{20})+eD_0x_{21}$$
$$+eD_1x_{20}+3d_2x_{20}^2x_{21}+fx_{21}+\lambda I_1=0, \tag{12b}$$

$$D_0I_1+D_1I_0+\zeta_1I_1-\zeta_2D_0x_{21}-\zeta_2D_1x_{20}=0. \tag{12c}$$

The general solution of Eq. (10) is given by

$$x_{10}(T_0,T_1)=A_1(T_1)\,\mathrm{e}^{\mathrm{i}\omega T_0}+\mathrm{cc}, \tag{13}$$

where cc represents the conjugate term, and A_1 represents the slowly varying amplitude of the primary structure. Assuming that the VNES will have 1:1 internal resonance, and will oscillate with frequency ω. The assumed solutions for the first order relative motion and current can be written as

$$x_{20}(T_0,T_1)=B_1(T_1)\,\mathrm{e}^{\mathrm{i}\omega T_0}+\mathrm{cc},$$
$$I_0(T_0,T_1)=\frac{\mathrm{i}\omega\zeta_2}{\mathrm{i}\omega+\zeta_1}B_1(T_1)\,\mathrm{e}^{\mathrm{i}\omega T_0}+H_1(T_1)\,\mathrm{e}^{-\zeta_1T_0}+\mathrm{cc}, \tag{14}$$

where B_1 denotes the slowly varying amplitude of VNES.

Substitute Eqs. (13) and (14) into Eq. (11b). Then the harmonic balance method is used for the frequency element of $\mathrm{e}^{\mathrm{i}\omega T_0}$. Higher order frequencies (3ω, 5ω) are not considered here. One arrives at

$$-\rho\omega^2A_1-\rho\omega^2B_1+fB_1+3d_2B_1^2\overline{B_1}+\mathrm{i}e\omega B_1$$
$$+\frac{\mathrm{i}\lambda\omega\zeta_2}{\mathrm{i}\omega+\zeta_1}B_1+\frac{\rho F}{2}\,\mathrm{e}^{\mathrm{i}\gamma W(T_1)}=0. \tag{15}$$

Further perturbation is used to get the fast dynamics. Substituting Eqs. (13) and (14) into Eq. (11a), one finds

$$D_0^2x_{11}+\omega^2x_{11}$$
$$=d_2B_1^3\,\mathrm{e}^{3\mathrm{i}\omega T_0}+\lambda H_1\,\mathrm{e}^{-\zeta_1T_0}$$
$$-\Big[\sigma A_1-\mathrm{i}e\omega B_1+2\mathrm{i}\omega D_1A_1+\mathrm{i}d_1\omega A_1-fB_1-3d_2B_1^2\overline{B_1}$$
$$-\frac{\mathrm{i}\lambda\omega\zeta_2}{\mathrm{i}\omega+\zeta_1}B_1+\frac{F}{2}\,\mathrm{e}^{\mathrm{i}\gamma W(T_1)}\Big]\,\mathrm{e}^{\mathrm{i}\omega T_0}+\mathrm{cc}. \tag{16}$$

Eliminating the secular terms of Eq. (16), one reads

$$D_1A_1=\frac{1}{4\omega}\Big[2\mathrm{i}\sigma A_1+2e\omega B_1-2d_1\omega A_1-2\mathrm{i}fB_1$$
$$-6\mathrm{i}d_2B_1^2\overline{B_1}+\frac{2\lambda\omega\zeta_2}{\mathrm{i}\omega+\zeta_1}B_1+\mathrm{i}F\,\mathrm{e}^{\mathrm{i}\gamma W(T_1)}\Big]. \tag{17}$$

Then Eq. (16) can be reduced as

$$D_0^2x_{11}+\omega^2x_{11}-d_2B_1^3\,\mathrm{e}^{3\mathrm{i}\omega T_0}-\lambda H_1\,\mathrm{e}^{-\zeta_1T_0}+\mathrm{cc}=0. \tag{18}$$

The particular solution of Eq. (18) is

$$x_{11}=-\frac{d_2B_1^3}{8\omega^2}\,\mathrm{e}^{3\mathrm{i}\omega T_0}+\frac{\lambda H_1}{\zeta_1^2+\omega^2}\,\mathrm{e}^{-\zeta_1T_0}+\mathrm{cc}. \tag{19}$$

Similar to the above analysis method, a solution for the response of the relative displacement is described as

$$x_{21}=B_2(T_1)\,\mathrm{e}^{\mathrm{i}\omega T_0}+\mathrm{cc}. \tag{20}$$

Substituting Eqs. (13), (14), (19) and (20) into Eq. (12b) and neglecting the higher order terms, we can obtain

$$-\rho\omega^2B_2+2\mathrm{i}\rho\omega D_1A_1+2\mathrm{i}\rho\omega D_1B_1+\mathrm{i}e\omega B_2$$
$$+eD_1B_1+fB+6d_2B_1B_2\overline{B_1}+3d_2B_1^2\overline{B_2}=0. \tag{21}$$

Multiplying Eq. (21) by ε and adding it to Eq. (15) lead to

$$-\rho\omega^2(B_1+\varepsilon B_2)+f(B_1+\varepsilon B_2)+\mathrm{i}e\omega(B_1+\varepsilon B_2)$$
$$+3d_2(B_1^2\overline{B_1}+\varepsilon B_1^2\overline{B_2}+2\varepsilon B_1B_2\overline{B_1})+2\mathrm{i}\varepsilon\rho\omega D_1A_1$$
$$+2\mathrm{i}\varepsilon\rho\omega D_1B_1+\varepsilon eD_1B_1+\frac{\mathrm{i}\lambda\omega\zeta_2}{\mathrm{i}\omega+\zeta_1}B_1$$
$$-\rho\omega^2A_1+\frac{\rho F}{2}\,\mathrm{e}^{\mathrm{i}\gamma W(T_1)}=0. \tag{22}$$

Letting $B=B_1+\varepsilon B_2$, $\dot{B}_1\approx\varepsilon D_1B_1$, $\dot{A}_1\approx\varepsilon D_1A_1$, $\varepsilon B_2\cong0$, equation (22) can be written by true time

$$(e+2\mathrm{i}\rho\omega)\dot{B}+2\mathrm{i}\rho\omega\dot{A}_1+3d_2B^2\overline{B}$$
$$+\left(-\rho\omega^2+\mathrm{i}e\omega+f+\frac{\mathrm{i}\lambda\omega\zeta_2}{\mathrm{i}\omega+\zeta_1}\right)B$$
$$+\frac{\rho F}{2}\,\mathrm{e}^{\mathrm{i}\gamma W(T_1)}-\rho\omega^2A_1=0. \tag{23}$$

The perturbation process is truncated at order ε of the system, then the solvability condition of Eq. (17) can be written by true time

$$\dot{A}_1=\frac{1}{4\omega}\Big(2\mathrm{i}\sigma A_1+2e\omega B-2d_1\omega A_1-2\mathrm{i}fB$$
$$-6\mathrm{i}d_2B^2\overline{B}+\frac{2\lambda\omega\zeta_2}{\mathrm{i}\omega+\zeta_1}B+\mathrm{i}F\,\mathrm{e}^{\mathrm{i}\gamma W(T_1)}\Big). \tag{24}$$

To simplify Eqs. (23) and (24), it is natural to assume

$$A_1(T_1)=\frac{1}{2}a(t)\,\mathrm{e}^{\mathrm{i}\alpha(t)},\quad B(T_1)=\frac{1}{2}b(t)\,\mathrm{e}^{\mathrm{i}\beta(t)}. \tag{25}$$

Substituting Eq. (25) into Eqs. (23) and (24) results in

$$8\rho\omega\,\mathrm{e}^{\mathrm{i}(\alpha-\beta)}\left(-\frac{1}{2}\omega a+\mathrm{i}\dot{a}-\dot{\alpha}a\right)$$
$$=-4(e+2\mathrm{i}\rho\omega)\dot{b}-4(\mathrm{i}e-2\rho\omega)b\dot{\beta}$$
$$-4\left(\frac{3}{4}d_2b^2-\rho\omega^2+\mathrm{i}e\omega+f+\frac{\mathrm{i}\lambda\omega\zeta_2}{\mathrm{i}\omega+\zeta_1}\right)b$$
$$-4\rho F\,\mathrm{e}^{\mathrm{i}(\gamma W(T_1)-\beta)},$$
$$8\omega\,(\dot{a}+\mathrm{i}a\dot{\alpha})\,\mathrm{e}^{\mathrm{i}\alpha}$$
$$=b\,\mathrm{e}^{\mathrm{i}\beta}\left(4e\omega-4\mathrm{i}f-3\mathrm{i}d_2b^2+\frac{4\lambda\omega\zeta_2}{\mathrm{i}\omega+\zeta_1}\right)$$
$$+4a\,\mathrm{e}^{\mathrm{i}\alpha}(\mathrm{i}\sigma-d_1\omega)+4\mathrm{i}F\,\mathrm{e}^{\mathrm{i}\gamma W(T_1)}. \tag{26}$$

Separating the real and imaginary parts of Eq. (26), the following four first-order nonlinear equations will be obtained:

$$\dot{a}=\frac{b}{2}\left(e+\frac{\lambda\zeta_1\zeta_2}{\omega^2+\zeta_1^2}\right)\cos(\beta-\eta)$$

$$
\begin{aligned}
&+\frac{b}{8\omega}\left(4f+3b^2d_2+\frac{4\lambda\omega^2\zeta_2}{\omega^2+\zeta_1^2}\right)\sin(\beta-\eta)\\
&+\frac{1}{2\omega}\left(F\sin\eta-ad_1\omega\right),\\
\dot{\eta} \;=\;& \frac{b}{2a}\left(e+\frac{\lambda\zeta_1\zeta_2}{\omega^2+\zeta_1^2}\right)\sin(\beta-\eta)\\
&-\frac{b}{8a\omega}\left(4f+3b^2d_2+\frac{4\lambda\omega^2\zeta_2}{\omega^2+\zeta_1^2}\right)\cos(\beta-\eta)\\
&+\frac{1}{2\omega a}[a\sigma+F\cos\eta-\gamma\dot{W}(T_1)],\\
\dot{b} \;=\;& \frac{1}{e^2+4\rho^2\omega^2}\left\{2\rho\left[\rho\omega^2d_1+\frac{1}{2}e(\omega^2+\sigma)\right]a\cos(\eta-\beta)\right.\\
&+2\rho\omega\left[(\omega^2+\sigma)\rho-\frac{1}{2}d_1e\right]a\sin(\eta-\beta)\\
&-e(1+\rho)\left(\frac{3}{4}b^2d_2+f+\frac{\lambda\omega^2\zeta_2}{\omega^2+\zeta_1^2}\right)b\\
&\left.-2\rho\omega(1+\rho)\frac{\lambda\omega\zeta_2^2}{\omega^2+\zeta_1^2}b-e\rho\omega^2(1+2\rho)b\right\},\\
\dot{\beta} \;=\;& \frac{1}{b(e^2+4\rho^2\omega^2)}\left\{-2\rho\omega\left[(\omega^2+\sigma)\rho-\frac{1}{2}d_1\lambda\right]\right.\\
&\times a\cos(\eta-\beta)+2\rho\left[\rho\omega^2d_1+\frac{1}{2}e(\omega^2+\sigma)\right]\\
&\times a\sin(\eta-\beta)-2\rho\omega(1+\rho)\left(\frac{3}{4}b^2d_2+f+\frac{\lambda\omega^2\zeta_2}{\omega^2+\zeta_1^2}\right)b\\
&\left.-\lambda(1+\rho)\frac{\lambda\omega\zeta_2^2}{\omega^2+\zeta_1^2}b-e^2(1+\rho)\omega b-2\rho^2\omega^3b\right\}, \qquad (27)
\end{aligned}
$$

where $\eta=\alpha-\gamma W(T_1)$. Solve Eq. (27) for the amplitudes a, b and the phases η, β. Combining Eqs. (8), (13), (14), and (25), the first-order approximate solutions of Eq. (5) can be written as

$$
\begin{aligned}
&x_1(t)=a(\varepsilon t)\cos(\omega t+\eta(\varepsilon t))+O(\varepsilon),\\
&x_2(t)=b(\varepsilon t)\cos(\omega t+\beta(\varepsilon t))+O(\varepsilon),\\
&I_0(t)=\frac{\omega\zeta_2}{\sqrt{\zeta_1^2+\omega^2}}b(\varepsilon t)\cos(\omega t-\beta(\varepsilon t)-\theta)+O(\varepsilon), \qquad (28)
\end{aligned}
$$

where $\theta=\arctan(\zeta_2/\omega)$, $(\omega\neq 0)$.

The frequency response of the system will be investigated next. Firstly, when $\gamma=0$, there is no random excitation in Eq. (27). The deterministic steady-state solutions can be indicated by assuming $\dot{a}=0$, $\dot{\eta}=0$, $\dot{b}=0$, $\dot{\beta}=0$.

$$
\begin{aligned}
&\frac{b_0}{2}\left(e+\frac{\lambda\zeta_1\zeta_2}{\omega^2+\zeta_1^2}\right)\cos(\beta_0-\eta_0)\\
&+\frac{b_0}{8\omega}\left(4f+3b_0^2d_2+\frac{4\lambda\omega^2\zeta_2}{\omega^2+\zeta_1^2}\right)\sin(\beta_0-\eta_0)\\
&+\frac{1}{2\omega}(F\sin\eta_0-a_0d_1\omega)=0,\\
&\frac{b_0}{2a_0}\left(e+\frac{\lambda\zeta_1\zeta_2}{\omega^2+\zeta_1^2}\right)\sin(\beta_0-\eta_0)\\
&-\frac{b_0}{8a_0\omega}\left(4f+3b_0^2d_2+\frac{4\lambda\omega^2\zeta_2}{\omega^2+\zeta_1^2}\right)\cos(\beta_0-\eta_0)\\
&+\frac{1}{2\omega a_0}(a_0\sigma+F\cos\eta_0)=0,\\
&\frac{1}{e^2+4\rho^2\omega^2}\left\{2\rho\left[\rho\omega^2d_1+\frac{1}{2}e(\omega^2+\sigma)\right]a_0\cos(\eta_0-\beta_0)\right.\\
&+2\rho\omega\left[(\omega^2+\sigma)\rho-\frac{1}{2}d_1e\right]a_0\sin(\eta_0-\beta_0)\\
&-e(1+\rho)\left(\frac{3}{4}b_0^2d_2+f+\frac{\lambda\omega^2\zeta_2}{\omega^2+\zeta_1^2}\right)b_0\\
&\left.-2\rho\omega(1+\rho)\frac{\lambda\omega\zeta_2^2}{\omega^2+\zeta_1^2}b_0-e\rho\omega^2(1+2\rho)b_0\right\}=0,\\
&\frac{1}{b_0(e^2+4\rho^2\omega^2)}\left\{-2\rho\omega\left[(\omega^2+\sigma)\rho-\frac{1}{2}d_1\lambda\right]\right.\\
&\times a_0\cos(\eta_0-\beta_0)+2\rho\left[\rho\omega^2d_1+\frac{1}{2}e(\omega^2+\sigma)\right]\\
&\times a_0\sin(\eta_0-\beta_0)-2\rho\omega(1+\rho)\left(\frac{3}{4}b_0^2d_2+f+\frac{\lambda\omega^2\zeta_2}{\omega^2+\zeta_1^2}\right)b_0\\
&\left.-\lambda(1+\rho)\frac{\lambda\omega\zeta_2^2}{\omega^2+\zeta_1^2}b_0-e^2(1+\rho)\omega b_0-2\rho^2\omega^3b_0\right\}=0. \qquad (29)
\end{aligned}
$$

Then when $\gamma\neq 0$, the non-trivial steady state solutions of Eq. (27) can be expressed as

$$
\begin{aligned}
&a=a_0+a_1,\quad \eta=\eta_0+\eta_1,\\
&b=b_0+b_1,\quad \beta=\beta_0+\beta_1, \qquad (30)
\end{aligned}
$$

where a_1, b_1, η_1 and β_1 are perturbation terms. Substituting Eq. (30) into Eq. (27) and according to Eq. (29), one arrives at

$$
\begin{aligned}
&\dot{a}_1=b_{11}a_1+b_{12}\eta_1+b_{13}b_1+b_{14}\beta_1,\\
&\dot{\eta}_1=b_{21}a_1+b_{22}\eta_1+b_{23}b_1+b_{24}\beta_1-\gamma\dot{W}(T_1),\\
&\dot{b}_1=b_{31}a_1+b_{32}\eta_1+b_{33}b_1+b_{34}\beta_1,\\
&\dot{\beta}_1=b_{41}a_1+b_{42}\eta_1+b_{43}b_1+b_{44}\beta_1, \qquad (31)
\end{aligned}
$$

where

$$
\begin{aligned}
b_{11} \;=\;& -\frac{d_1}{2},\quad b_{12}=-\frac{a_0\sigma}{2\omega},\\
b_{13} \;=\;& \frac{3b_0^2d_2}{4\omega}\sin(\beta_0-\eta_0)\\
&+\left(4f+3b_0^2d_2+\frac{4\lambda\omega^2\zeta_2}{\omega^2+\zeta_1^2}\right)\frac{\sin(\beta_0-\eta_0)}{8\omega}\\
&+\left(e+\frac{\lambda\zeta_1\zeta_2}{\omega^2+\zeta_1^2}\right)\frac{\cos(\beta_0-\eta_0)}{2},\\
b_{14} \;=\;& \left(4f+3b_0^2d_2+\frac{4\lambda\omega^2\zeta_2}{\omega^2+\zeta_1^2}\right)\frac{b_0\cos(\beta_0-\eta_0)}{8\omega}\\
&-\left(e+\frac{\lambda\zeta_1\zeta_2}{\omega^2+\zeta_1^2}\right)\frac{b_0\sin(\beta_0-\eta_0)}{2},\\
b_{21} \;=\;& \frac{\sigma}{2a_0\omega},\quad b_{22}=b_{11},
\end{aligned}
$$

$$
\begin{aligned}
b_{23} &= \left(e+\frac{\lambda\zeta_1\zeta_2}{\omega^2+\zeta_1^2}\right)\frac{\sin(\beta_0-\eta_0)}{2a_0}\\
&\quad-\left(4f+3b_0^2d_2+\frac{4\lambda\omega^2\zeta_2}{\omega^2+\zeta_1^2}\right)\frac{\cos(\beta_0-\eta_0)}{8\omega a_0}\\
&\quad-\frac{3b_0^2d_2}{4\omega a_0}\cos(\beta_0-\eta_0),\\
b_{24} &= \left(e+\frac{\lambda\zeta_1\zeta_2}{\omega^2+\zeta_1^2}\right)\frac{b_0\cos(\beta_0-\eta_0)}{2a_0}\\
&\quad+\left(4f+3b_0^2d_2+\frac{4\lambda\omega^2\zeta_2}{\omega^2+\zeta_1^2}\right)\frac{b_0\sin(\beta_0-\eta_0)}{8\omega a_0},\\
b_{31} &= \left(\frac{2\rho(\rho\omega^2d_1+\frac{1}{2}e(\omega^2+\sigma))}{e^2+4\rho^2\omega^2}\right)\cos(\beta_0-\eta_0)\\
&\quad-\left(\frac{2\rho\omega((\omega^2+\sigma)\rho-\frac{1}{2}ed_1)}{e^2+4\rho^2\omega^2}\right)\sin(\beta_0-\eta_0),\\
b_{32} &= \frac{2\rho(\rho\omega^2d_1+\frac{1}{2}e(\omega^2+\sigma))a_0\sin(\beta_0-\eta_0)}{e^2+4\rho^2\omega^2}\\
&\quad+\frac{2\rho\omega((\omega^2+\sigma)\rho-\frac{1}{2}ed_1)a_0\cos(\beta_0-\eta_0)}{e^2+4\rho^2\omega^2},\\
b_{33} &= -\left(\frac{9}{4}b_0^2d_2+f+\frac{\lambda\omega^2\zeta_2}{\omega^2+\zeta_1^2}\right)\frac{e(1+\rho)}{e^2+4\rho^2\omega^2},\\
b_{34} &= -b_{32},\\
b_{41} &= -\left(\frac{2\rho\omega((\omega^2+\sigma)\rho-\frac{1}{2}d_1\lambda)}{e^2+4\rho^2\omega^2}\right)\frac{\cos(\beta_0-\eta_0)}{b_0}\\
&\quad-\left(\frac{2\rho(\rho\omega^2d_1+\frac{1}{2}e(\omega^2+\sigma))}{e^2+4\rho^2\omega^2}\right)\frac{\sin(\beta_0-\eta_0)}{b_0},\\
b_{42} &= -\left(\frac{2\rho\omega((\omega^2+\sigma)\rho-\frac{1}{2}d_1\lambda)}{e^2+4\rho^2\omega^2}\right)\frac{a_0\sin(\beta_0-\eta_0)}{b_0}\\
&\quad+\left(\frac{2\rho(\rho\omega^2d_1+\frac{1}{2}e(\omega^2+\sigma))}{e^2+4\rho^2\omega^2}\right)\frac{a_0\cos(\beta_0-\eta_0)}{b_0},\\
b_{43} &= \left(\frac{2\rho(\rho\omega^2d_1+\frac{1}{2}e(\omega^2+\sigma))}{e^2+4\rho^2\omega^2}\right)\frac{a_0\sin(\beta_0-\eta_0)}{b_0^2}\\
&\quad+\left(\frac{2\rho\omega((\omega^2+\sigma)\rho-\frac{1}{2}d_1\lambda)}{e^2+4\rho^2\omega^2}\right)\frac{a_0\cos(\beta_0-\eta_0)}{b_0^2}\\
&\quad+\frac{3\rho\omega(1+\rho)d_2b_0}{e^2+4\rho^2\omega^2},\\
b_{44} &= -b_{42}.
\end{aligned}
$$

Then, the second-order moments are derived and they should satisfy

$$
\begin{aligned}
\frac{\mathrm{d}E(a_1^2)}{\mathrm{d}T_1} &= \frac{\mathrm{d}E(a_1b_1)}{\mathrm{d}T_1}=\frac{\mathrm{d}E(a_1\eta_1)}{\mathrm{d}T_1}=\frac{\mathrm{d}E(a_1\beta_1)}{\mathrm{d}T_1}=\frac{\mathrm{d}E(b_1^2)}{\mathrm{d}T_1}\\
&= \frac{\mathrm{d}E(b_1\eta_1)}{\mathrm{d}T_1}=\frac{\mathrm{d}E(b_1\beta_1)}{\mathrm{d}T_1}=\frac{\mathrm{d}E(\eta_1^2)}{\mathrm{d}T_1}=\frac{\mathrm{d}E(\eta_1\beta_1)}{\mathrm{d}T_1}\\
&= \frac{\mathrm{d}E(\beta_1^2)}{\mathrm{d}T_1}=0. \qquad (32)
\end{aligned}
$$

According to Cramer's rule, the second-order steady-state moments can be obtained by solving the following linear algebra equations:

$$\boldsymbol{BX}=\boldsymbol{C}, \qquad (33)$$

where

$$\boldsymbol{X}=(E(a_1^2),E(a_1b_1),E(a_1\eta_1),E(a_1\beta_1),E(b_1^2),E(b_1\eta_1),E(b_1\beta_1),E(\eta_1^2),E(\eta_1\beta_1),E(\beta_1^2))^{\mathrm{T}},\ \boldsymbol{C}=(0,0,0,0,0,0,0,\gamma^2,0,0)^{\mathrm{T}},$$

$$
\boldsymbol{B}=\begin{pmatrix}
2b_{11} & 2b_{13} & 2b_{12} & 2b_{14} & 0 & 0 & 0 & 0 & 0 & 0\\
b_{31} & b_{11}+b_{33} & b_{32} & -b_{32} & b_{13} & b_{12} & b_{14} & 0 & 0 & 0\\
b_{21} & b_{23} & 2b_{11} & b_{24} & 0 & b_{13} & b_{12} & 0 & b_{14} & 0\\
b_{41} & b_{43} & b_{42} & b_{11}-b_{42} & 0 & 0 & b_{13} & 0 & b_{12} & b_{14}\\
0 & 2b_{31} & 0 & 0 & 2b_{33} & 2b_{32} & -2b_{32} & 0 & 0 & 0\\
0 & b_{21} & b_{31} & 0 & b_{23} & b_{11}+b_{33} & b_{24} & b_{32} & -b_{32} & 0\\
0 & b_{41} & 0 & b_{31} & b_{43} & b_{42} & b_{33}-b_{42} & 0 & b_{32} & -b_{32}\\
0 & 0 & 2b_{21} & 0 & 0 & 2b_{23} & 0 & 2b_{11} & 2b_{24} & 0\\
0 & 0 & b_{41} & b_{21} & 0 & b_{43} & b_{23} & b_{42} & b_{11}-b_{42} & b_{24}\\
0 & 0 & 0 & 2b_{41} & 0 & 0 & 2b_{43} & 0 & 2b_{42} & -2b_{42}
\end{pmatrix}.
$$

The moment method is employed to get the first-order and the second-order steady-state moments of the system and the output current as follows:

$$
\begin{aligned}
&E(a)=a_0,\ \ E(a^2)=a_0^2+E(a_1^2),\\
&E(b)=b_0,\ \ E(b^2)=b_0^2+E(b_1^2),\\
&E(I)=\frac{\omega\zeta_2}{\sqrt{\zeta_1^2+\omega^2}}b_0,\ \ E(I^2)=\frac{2\omega^2\zeta_2^2}{\zeta_1^2+\omega^2}(b_0^2+E(b_1^2)). \qquad (34)
\end{aligned}
$$

The mean output power is

$$EP=\lambda\zeta_1E(I^2). \qquad (35)$$

4. Results and discussion

4.1. Numerical verification

To verify the effectiveness of the multiple-scale method, numerical solutions of system (5) from the fourth-order

Runge–Kutta method and approximate analytical solutions obtained from Eq. (29) are compared in this subsection. Two sets of parameter values are selected, and the fitting image of the analytical and numerical solutions is plotted in Fig. 2. The solid lines represent approximate analytical solutions, and the dots are numerical solutions. Approximate analytical solutions and numerical solutions match very well in Fig. 2, which means the proposed method is effective.

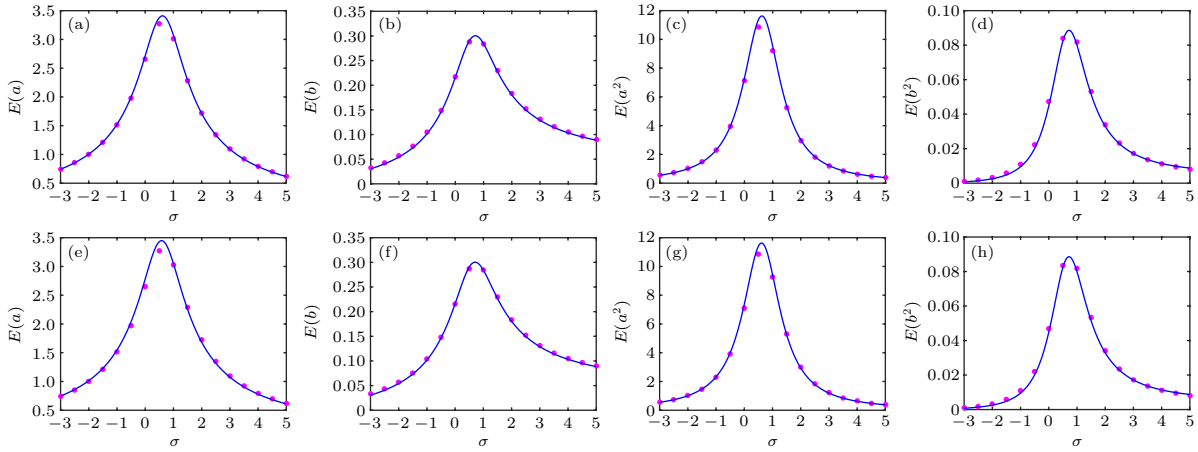


Fig. 2. Comparison between the approximate analytical solutions and numerical solutions. (a), (b), (e), (f) The first-order steady-state moment; (c), (d), (g), (h) the second-order steady-state moment.

4.2. Parameter analysis

The effects of different system parameters on amplitude-frequency responses of the primary structure and VNES are investigated, as plotted in Fig. 3.

The first-order steady-state moments of amplitudes $E(a)$ and $E(b)$ for different deterministic amplitudes F are depicted in Figs. 3(a) and 3(d). Increasing the value of F, the amplitudes of $E(a)$ and $E(b)$ also increase. This shows that the larger value of F will strengthen the vibration of the system.

For the system parameter mass ratio ρ, it can be seen from Figs. 3(b) and 3(e) that the amplitude of $E(a)$ decreases with the increase of ρ and the curves gradually shift to the right with the increase of ρ. The amplitude of $E(b)$ increases with the increase of ρ and the curve shifts to the right as ρ increases. That is to say, increasing the mass ratio of VNES to the primary structure is beneficial to weaken the vibration of the primary structure. But the increment of ρ is not beneficial to weaken the vibration of VNES. In order to balance the vibration suppression effect between the primary structure and VNES, the optimal mass ratio should be taken into account.

Then, the selection of linear damping coefficient d_4 is analyzed in Figs. 3(c) and 3(f). The larger the value of d_4, the bigger the amplitude of $E(a)$, the smaller the amplitude of $E(b)$. That is the increase of d_4 is not conducive to the stability of the primary structure, but is beneficial to the stability of VNES.

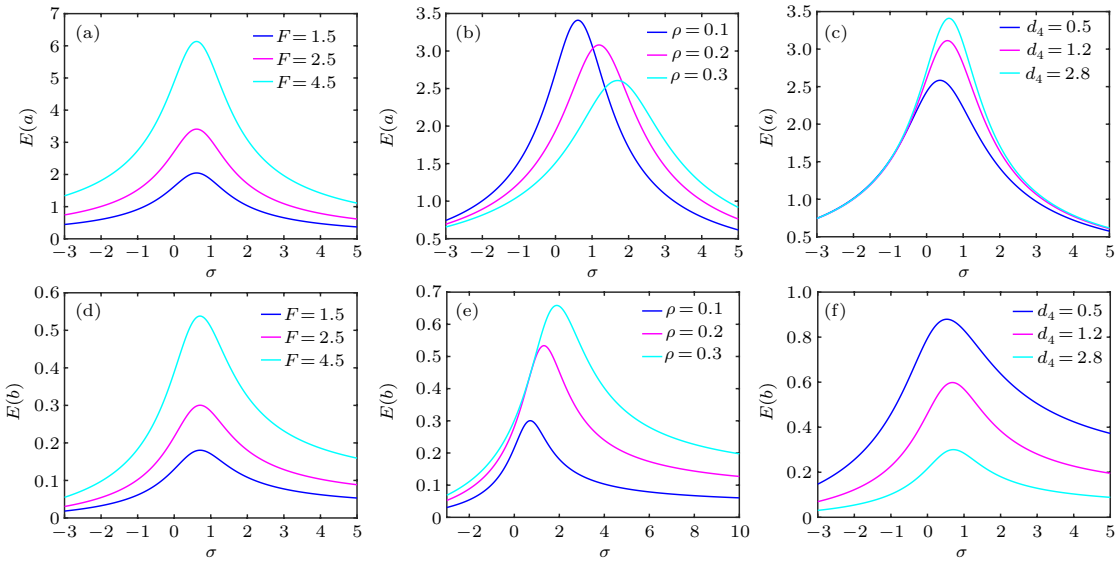


Fig. 3. The first-order steady-state moments of amplitudes $E(a)$ and $E(b)$ for different F, ρ, d_4. (a)–(c) The primary structure, (d)–(f) VNES.

4.3. Stochastic P-bifurcation

To further explore impacts of system parameters on system dynamic behavior, the steady-state probability density functions (SPDFs) of displacement are calculated by Monte Carlo numerical simulations. The stochastic P-bifurcation of an electromechanically coupled VNES model under narrow-band random excitation is essentially a transition of dynamic responses between a steady state and an unstable state, which will be directly expressed as follows. Fix $\varepsilon = 0.1$, $\mu = 0.2$, $\lambda = 0.2$, $\omega = 2.5$, $\sigma = 2.5$, $\rho = 0.1$, $\zeta_1 = 0.1$, $\zeta_2 = 4.0$, $d_1 = 0.3$. Furthermore, all of SPDFs of displacement are drawn under the same initial conditions $x_1(0) = 0$, $\dot{x}_1(0) = 0.01$, $x_2(0) = 0.01$, $\dot{x}_2(0) = 0.01$.

Firstly, one peak appears in Fig. 4(a) when $F = 0.3$, $\gamma = 1.55$, $d_2 = 0.5$, $d_3 = 0.1$, $d_4 = 2.8$. However, the appearance of double peaks can be caused by increasing the deterministic amplitude, where $F = 2.5$. That is, a jump phenomenon occurs at this moment. The phenomenon is also called stochastic P-bifurcation account for the number of the peak of SPDF changes.

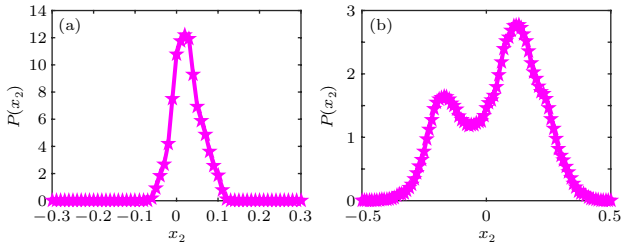


Fig. 4. Effect of deterministic amplitude F on SPDF of displacement. (a) $F = 0.3$, (b) $F = 2.5$.

Secondly, figure 5 illustrates that stochastic P-bifurcation can be induced by increasing noise intensity γ, where $F = 2.5$, $d_2 = 0.5$, $d_3 = 0.1$, $d_4 = 2.8$. With the increase of γ, the number of the peak of $P(x_2)$ transforms from one to two. Results reveal that the change of noise intensity makes stochastic P-bifurcation appear.

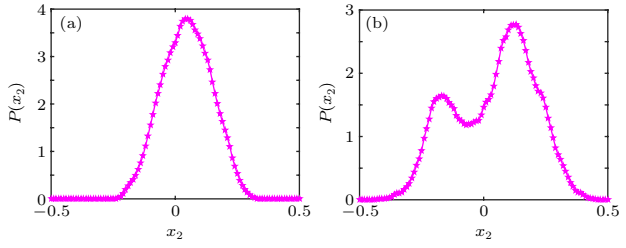


Fig. 5. Effect of noise intensity γ on SPDF of displacement. (a) $\gamma = 0.55$, (b) $\gamma = 1.55$.

Thirdly, figure 6 shows the transformation of the shape of $P(x_2)$ from a bimodal structure to a unimodal structure as the cubic stiffness coefficient d_2 increases, where $F = 2.5$, $\gamma = 1.55$, $d_3 = 0.1$, $d_4 = 2.8$. Conclusions come that d_2 can give rise to the appearance of stochastic P-bifurcation.

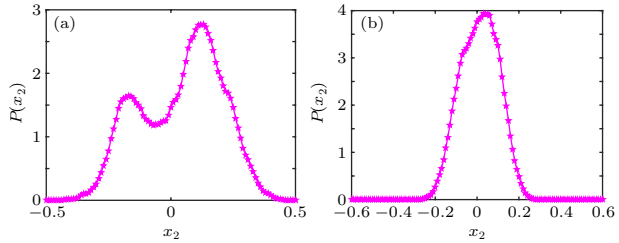


Fig. 6. Effect of cubic stiffness coefficient d_2 on SPDF of displacement. (a) $d_2 = 0.5$, (b) $d_2 = 5.0$.

Fourthly, figure 7 describes the structure of $P(x_2)$ varies from bimodal to unimodal as fractional-order damping coefficient d_3 increases, where $F = 2.5$, $\gamma = 1.55$, $d_2 = 0.5$, $d_4 = 2.8$. Consequences verify that d_3 can lead to the appearance of stochastic P-bifurcation.

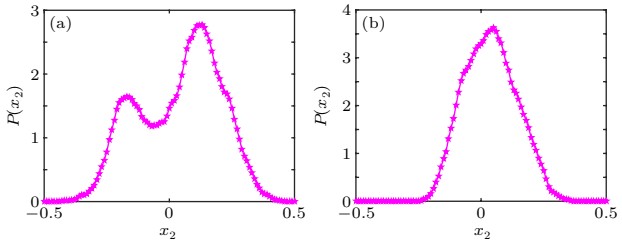


Fig. 7. Effect of fractional-order damping coefficient d_3 on SPDF of displacement. (a) $d_3 = 0.1$, (b) $d_3 = 4.0$.

Lastly, figure 8 presents that the configuration of $P(x_2)$ changes from unimodal to bimodal when linear damping coefficient d_4 increases, where $F = 2.5$, $\gamma = 1.55$, $d_2 = 0.5$, $d_3 = 0.1$. This demonstrates that stochastic P-bifurcation can be induced by d_4.

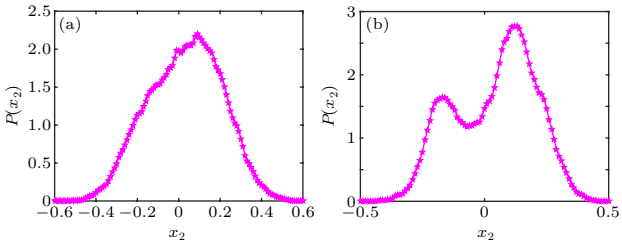


Fig. 8. Effect of linear damping coefficient d_4 on SPDF of displacement. (a) $d_4 = 1.0$, (b) $d_4 = 2.8$.

4.4. Energy harvesting performance

To evaluate the efficiency of electromagnetic energy harvesting, the influences of system parameters on the mean square current $E(I^2)$ and mean output power $E(P)$ are analyzed and plotted in Figs. 9–16.

Firstly, with increase of both cubic stiffness coefficient d_2 and noise intensity γ, the values of $E(I^2)$ and $E(P)$ also increase as shown in Fig. 9. By observing Figs. 10 and 11, it can be seen that with the increase of electromagnetic coupling coefficient ζ_2 and mass ratio ρ, $E(I^2)$, $E(P)$ and ζ_2 show an exponential growth trend. These illustrate that larger d_2, ζ_2, ρ and γ are benefit to energy harvesting.

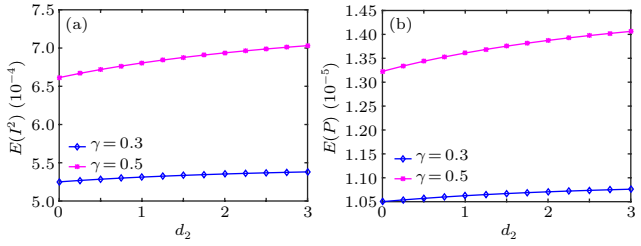


Fig. 9. Variation of mean square current and mean output power with respect to d_2 for different γ values. (a) $E(I^2)$, (b) $E(P)$.

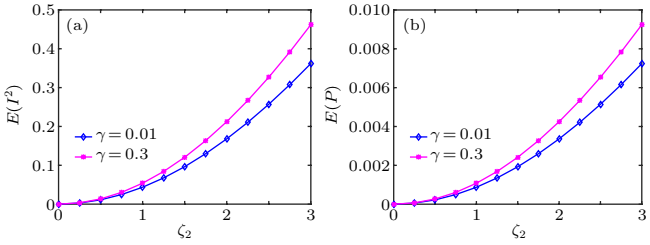


Fig. 10. Variation of mean square current and mean output power with respect to ζ_2 for different γ values. (a) $E(I^2)$, (b) $E(P)$.

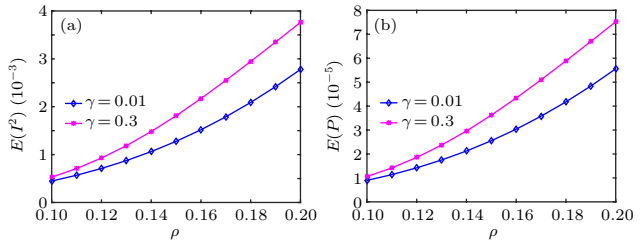


Fig. 11. Variation of mean square current and mean output power with respect to ρ for different γ values. (a) $E(I^2)$, (b) $E(P)$.

Secondly, figures 12–14 illustrate that $E(I^2)$ and $E(P)$ decrease significantly with the increase of fractional-order damping d_3, fractional derivative order μ and linear damping of VNES d_4 coefficients, while increase with the increase of noise intensity γ. This shows that the smaller d_3, d_4, and μ, the better the energy harvesting performance.

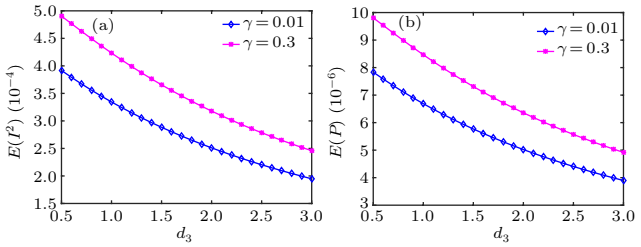


Fig. 12. Variation of mean square current and mean output power with respect to d_3 for different γ values. (a) $E(I^2)$, (b) $E(P)$.

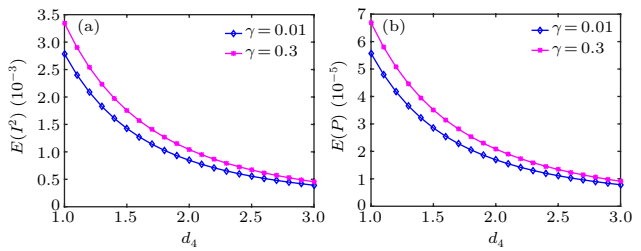


Fig. 13. Variation of mean square current and mean output power with respect to d_4 for different γ values. (a) $E(I^2)$, (b) $E(P)$.

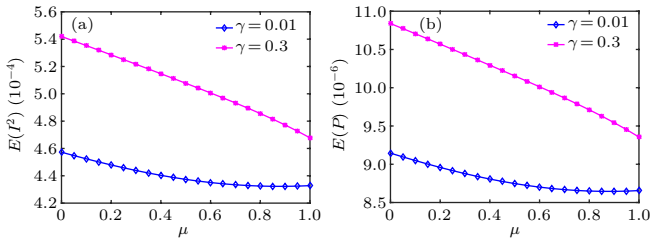


Fig. 14. Variation of mean square current and mean output power with respect to μ for different γ values. (a) $E(I^2)$, (b) $E(P)$.

Thirdly, figure 15 shows that $E(I^2)$ increases with the increase of electromechanical coupling coefficient λ and noise intensity γ, while $E(P)$ increases directly with the increase of λ. That is to say, the larger λ, the larger $E(I^2)$ and $E(P)$, the better the energy harvesting performance of the system.

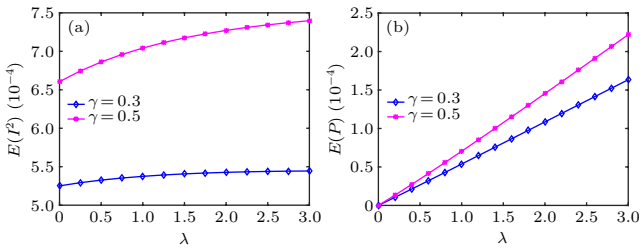


Fig. 15. Variation of mean square current and mean output power with respect to λ for different γ values. (a) $E(I^2)$, (b) $E(P)$.

Lastly, figure 16 describes that $E(I^2)$ decreases with increasing the ratio between resistance and inductance ζ_1, while $E(P)$ first increases significantly and then decreases slightly. It shows that there exists an optimal solution for ζ_1 to maximize the energy harvesting performance of the system. Besides, it can be seen from the figure that under the conditions of this paper, the optimal value of ζ_1 is between 2.4 and 2.8.

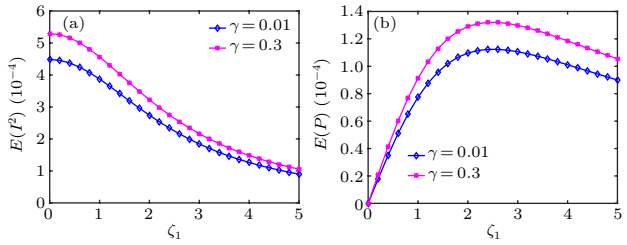


Fig. 16. Variation of mean square current and mean output power with respect to ζ_1 for different γ values. (a) $E(I^2)$, (b) $E(P)$.

5. Conclusions

This paper explored the amplitude–frequency responses, stochastic P-bifurcation, and energy harvesting performance of an electromagnetic energy harvester enhanced viscoelastic nonlinear energy sink system under narrow-band random excitation. These aspects were investigated using the multiple-scale method. The effectiveness of this method was verified through Monte Carlo simulation.

Through studying the effects of deterministic amplitude F, the mass ratio of VNES to the primary structure ρ and lin-

ear damping coefficient of VNES d_4 on the first-order steady-state moment of VNES, we observed that decreasing F and d_4 enhances the vibration suppression performance of VNES, while increasing ρ has the opposite effect. In addition, it was observed that decreasing both cubic stiffness coefficient d_2 and fractional-order damping coefficient d_3 can lead to the occurrence of stochastic P-bifurcation. Moreover, the values of F, the intensity of Gaussian white noise γ and d_4 should be decreased to prevent stochastic P-bifurcation.

The effects of system parameters on the mean square current $E(I^2)$ and mean output power $E(P)$ were discussed. It was concluded that the energy harvesting performance of the system can be improved by increasing γ, d_2, electromechanical coupling coefficient λ and electromagnetic coupling coefficient ζ_2, and by decreasing d_3 and fractional derivative order μ. Furthermore, there exists an optimal value of the ratio between resistance and inductance ζ_1, as $E(I^2)$ decreases with the increase of ζ_1, while $E(P)$ increases first and then decreases with the increase of ζ_1.

Acknowledgments

Project supported by the National Natural Science Foundation of China (Grant No. 12002089), the Science and Technology Projects in Guangzhou (Grant No. 2023A04J1323), and UKRI Horizon Europe Guarantee (Grant No. EP/Y016130/1).

References

[1] Wang L, Zhou Y, Nagarajaiah S and Shi W 2023 *Engineering Structures* **294** 116744
[2] Araz O, Elias S and Kablan F 2023 *Soil Dynamics and Earthquake Engineering* **166** 107765
[3] Gatti G and Svelto C 2023 *Journal of Vibration and Control* **29** 5713
[4] Ali A, Ahmed A, Ali M, Azam A, Wu X, Zhang Z and Yuan Y 2023 *Environmental Science and Pollution Research* **30** 5371
[5] Shen R, Qian X, Zhou J and Lee C 2023 *Journal of Vibration and Control* **29** 5078
[6] Vakakis A F 2001 *J. Vib. Acoust.* **123** 324
[7] Vakakis A F and Gendelman O 2001 *J. Appl. Mech.* **68** 42
[8] Saeed A S, Abdul Nasar R and ALshudeifat M A 2023 *Nonlinear Dynam.* **111** 1
[9] Ding H and Chen L Q 2020 *Nonlinear Dynam.* **100** 3061
[10] Wang Y, Kang H, Cong Y, Guo T and Zhu W 2023 *Communications in Nonlinear Science and Numerical Simulation* **117** 106988
[11] Wang F, Yang Y, Zeng J, Yang Y and Li Y 2023 *Archive of Applied Mechanics* **93** 4241
[12] Zeng Y, Ding H, Ji J, Jing X and Chen L 2023 *Mechanical Systems and Signal Processing* **202** 110694
[13] Sui P, Shen Y and Wang X 2023 *Nonlinear Dynam.* **111** 7157
[14] Li S and Ding H 2023 *International Journal of Dynamics and Control* **12** 1671
[15] Zhang Y, Kong X, Yue C and Guo J 2023 *Nonlinear Dynam.* **111** 15817
[16] Ding H and Shao Y 2022 *Applied Mathematics and Mechanics* **43** 1793
[17] Zhang W, Zhang W and Guo X 2023 *Applied Mathematics and Mechanics* **44** 1721
[18] Zhang Y, Kong X and Yue C 2023 *Communications in Nonlinear Science and Numerical Simulation* **116** 106837
[19] Li S and Ding H 2023 *Nonlinear Dynam.* **111** 18605
[20] Gaidai O, Gu Y, Xing Y, Wang J and Yurchenko D 2023 *Theoretical and Applied Mechanics Letters* **13** 100422
[21] Bergeot B 2023 *International Journal of Non-Linear Mechanics* **150** 104351
[22] Carvalho E M and Kumar S 2023 *Acta Biomaterialia* **163** 146
[23] Yang Y, Huang M, Guo S and Sun Y 2023 *Mechanical Systems and Signal Processing* **186** 109837
[24] Sharma P and Diebels S 2023 *Journal of Materials Science* **58** 6254
[25] Huang D, Li R and Yang G 2019 *Communications in Nonlinear Science and Numerical Simulation* **79** 104916
[26] Hu H, Chen L and Qian J 2023 *Journal of Vibration and Control* 1
[27] Moslemi A and Homaeinezhad M 2023 *Applied Mathematics and Mechanics* **44** 141
[28] Liu L, He L, Han Y, Zheng X, Sun B and Cheng G 2023 *Sensors and Actuators A: Physical* **349** 114054
[29] Li J, Wang G, Yang P, Wen Y, Zhang L, Song R and Hou C 2024 *Energy* **286** 129578
[30] Chen L, Ma Y, Hou C, Su X and Li H 2023 *Applied Mathematical Modelling* **116** 350
[31] Sun Y H, Zeng Y H and Yang Y G 2024 *Acta Mechanica Sinica* **40** 523154
[32] Han J, Huang D, Li W, Yang G and Gubeljak N 2023 *International Journal of Non-Linear Mechanics* **157** 104518
[33] Huang D, Han J, Li W, Deng H and Zhou S 2023 *Communications in Nonlinear Science and Numerical Simulation* **119** 107086
[34] Franzini G R, Maciel V S F, Vernizzi G J and Zulli D 2023 *Nonlinear Dynam.* **111** 22215
[35] Zhang H, Li Z, Yang Z and Zhou S 2023 *Communications in Nonlinear Science and Numerical Simulation* **125** 107350
[36] Li M, Yu D, Li Y, Liu X and Dai F 2023 *International Journal of Non-Linear Mechanics* **156** 104464
[37] Starosvetsky Y and Gendelman O 2010 *Nonlinear Dynam.* **59** 711
[38] Zang J and Zhang Y 2019 *Nonlinear Dynam.* **98** 889
[39] Mirhashemi S, Saeidiha M and Ahmadi H 2023 *Communications in Nonlinear Science and Numerical Simulation* **118** 107035
[40] Sun Y H, Liao Z J and Yang Y G 2024 *Nonlinear Dynam.* 1
[41] Xiong L, Tang L, Liu K and Mace B R 2018 *J. Phys. D: Appl. Phys.* **51** 185502
[42] Kremer D and Liu K 2017 *Journal of Sound and Vibration* **410** 287
[43] Zulli D and Luongo A 2015 *Meccanica* **50** 781
[44] Yang Y, Xu W, Yang G and Jia W 2016 *Chaos* **26** 084302